Petroleum Science 23 (2026) 245–261

Contents lists available at ScienceDirect

Petroleum Science

journal homepage: www.keaipublishing.com/en/journals/petroleum-science

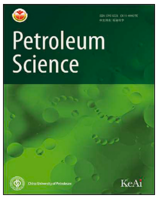

Original Paper

Hydrodynamics characteristics of rough-walled self-propping shale fractures: from microscale morphology to macroscale hydraulic response

Ming-Yong Zeng [a,*], Hang-Yu Zhou [b,**]

[a] *Petroleum Engineering Technology Institute of Southwest Petroleum Branch, SINOPEC, Deyang, 618000, Sichuan, China*
[b] *National Key Laboratory of Oil and Gas Reservoir Geology and Exploitation, Southwest Petroleum University, Chengdu, 610500, Sichuan, China*

A R T I C L E I N F O

Article history:
Received 26 May 2025
Received in revised form
16 October 2025
Accepted 17 October 2025
Available online 24 October 2025

Edited by Jia-Jia Fei

Keywords:
Shale
Self-propping fractures
Fractal dimension
Multi-scale morphology
Fracture conductivity

A B S T R A C T

Self-propping fractures formed during hydraulic fracturing in shale reservoirs constitute a critical component of the hydraulic fractures, with surface roughness serving as a pivotal factor governing their mechanical and hydraulic properties. To examine the regulatory effects and underlying mechanisms of rough morphology on fluid transport behavior within self-propping fractures under closure stress, this study employs the fast Fourier transform (FFT) method to generate synthetic rough fractures characterized by fractal Brownian motion (FBM) features. Subsequently, a coupled mechanical-hydraulic model for single rough self-propping fractures was established to simulate the influence of morphological roughness on their hydrodynamics characteristics. The results demonstrate that under closure stress, the deformation increment of self-propping fractures exhibits a pronounced synchronous relationship with fracture conductivity degradation. The progressive narrowing of fracture aperture induced by increasing closure stress constitutes the primary mechanism driving persistent conductivity deterioration. Furthermore, both high-density "cluster-like" contact micro-asperities and "throat-shaped" constriction structures have been identified as critical morphological factors. Regions dominated by the high-density "cluster-like" contact micro-asperities significantly constrict the flow pathways, inducing specialized flow phenomena such as "transverse flow" and "reverse flow". Concurrently, the "throat-shaped" constriction structures generate significant throttling effects, precipitating abrupt pressure drops. These combined mechanisms fundamentally degrade the conductivity of self-propping fractures under closure stress. A linear positive correlation exists between fractal dimension and fracture conductivity. While closure stress induces significant reconfiguration of flow pathways, the interplay between fractal roughness characteristics and stress-induced deformation preserves the integrity of favorable flow conduits, resulting in higher conductivity with larger fractal dimensions. Fracture conductivity is governed by the competitive interaction between the roughness-mediated reduction in flow resistance and the throat constriction effect during mechanical compression. The primary flow pathways within self-propping fractures are predominantly dictated by the fundamental large-scale morphological structures. In contrast, small-scale roughness features primarily enhance flow heterogeneity in velocity magnitude and direction. Crucially, these secondary structures do not fundamentally alter the spatial distribution pattern of the primary flow channels in self-propping fractures.

1. Introduction

The shale oil and gas resource endowment in China is manifested through the widespread distribution of organic-rich shales across marine, continental, and marine-continental transitional facies, which has emerged as a strategic priority for exploration and development (Guo et al., 2025). Breakthroughs and the

---

* Corresponding author.
** Corresponding author.

E-mail addresses: 562304475@qq.com (M.-Y. Zeng), hangyu_zhou999@163.com (H.-Y. Zhou).

Peer review under the responsibility of China University of Petroleum (Beijing).

https://doi.org/10.1016/j.petsci.2025.10.015

widespread application of multi-stage hydraulic fracturing in horizontal wells have significantly accelerated the shale oil and gas industry's development (Sun et al., 2023). The complex fracture networks within these reservoirs serve as primary flow channels for hydrocarbons (Wu et al., 2024; Finenko and Konietzky, 2024). However, the majority of fractures in these networks are not propped by proppants, and forming self-propping fractures (Cipolla et al., 2009). Although self-propping fractures exhibit relatively lower conductivity compared to propped fractures, they remain essential components of the overall flow capacity within complex fracture networks (Sharma and Manchanda, 2015). Critically, these self-propping fractures play a pivotal role in sustaining connectivity between complex fracture networks and the formation matrix (Britt et al., 2006), thereby ensuring sufficient production rates even in regions with low proppants placement (Julia et al., 2014).

The investigation of hydrodynamics within complex artificial fracture networks is a critical focus in fracture conductivity construction. However, constrained by inherent uncertainties in fracture networks morphology and limitations in computational capabilities, existing researches have primarily focused on hydrodynamics phenomena in single rough fracture (Zhong et al., 2021; Deng et al., 2021). This simplified approach has been extensively applied in various fields, including oil and gas production (Xie et al., 2020), geothermal energy development (Huang et al., 2021), carbon dioxide sequestration (Nasvi et al., 2013), and contaminant and nuclear waste disposal (Medici et al., 2019). These studies demonstrate that the hydrodynamics characteristics within rough-walled fractures are strongly dependent on both the roughness morphology of the fracture surfaces (Lu et al., 2021; Zhu et al., 2022) and the contact characteristics resulting from surface stress (Wang et al., 2024; Blöcher et al., 2019). Tzelepis et al. (2015) revealed that the hydraulic head loss during fluid flow through rock fractures exhibits a positive correlation with fracture surface roughness magnitude. Xiao and Zhao (2019) evaluated the influence of surface roughness on fluid flow by comparing the equivalent hydraulic apertures under different conditions, revealing a negative correlation between surface roughness and the equivalent hydraulic aperture. Hu et al. (2024) investigated the hydrodynamics behavior in fractures with distinct fractal dimensions, finding that the equivalent permeability decreases linearly with increasing fractal dimension. Cheng et al. (2024) observed that fluid flow rate progressively decreases under a constant pressure gradient as fractal dimension increases in fractures exhibiting fractal roughness. Furthermore, Kong and Chen (2018) established a fracture geometric model utilizing a high-resolution optical profilometer to simulate the influence of rough structures on fracture conductivity. The tortuous pathways of fluid flow attributed to heterogeneous fractures width distribution. Guo et al. (2020) developed a full-field fracture flow visualization experiment, identifying the occurrence of backflow and vortex phenomena induced by localized rough structures. Rong et al. (2020) experimentally investigated the relationship between fracture flow and surface roughness, revealing that fractures exhibit significant permeability only when their aperture surpasses a critical threshold. The highly disordered and complex fracture morphology results in complex fluid motion within rough-walled fractures (Li et al., 2024). Consequently, surface roughness reduces fracture flow capacity (Yang et al., 2023), while the irregular and heterogeneous distribution of these features significantly complicates flow dynamics (Xu et al., 2018). This enhanced flow pathways tortuosity promotes preferential flow channel development and induces significant fluid disturbances (Xu et al., 2024). Such disturbances manifest as specialized flow phenomena including bypass flow, transverse flow, and vortex (Zhan et al., 2022), collectively resulting in a marked reduction in fracture flow capacity. Although extensively studied, existing research has predominantly focused on quantifying and characterizing the influence of fracture surface roughness on flow capacity and its variation patterns. However, the underlying mechanisms by which microscopic topographical variations govern macro-scale flow regimes remain incompletely understood.

In reality, the majority of rock fractures within in-situ formations remain partially closed to withstand in-situ stresses (Su et al., 2024). Stress perturbations can induce alterations in fracture aperture geometry, thereby influencing hydrodynamics within rough-walled fractures (Dapp et al., 2012). Chen et al. (2019) observed through experimental investigations that the fracture flow capacity of shale fractures decreases by orders of magnitude with increasing closure stress. Similarly, Zhao et al. (2020) observed a substantial reduction in the flow capacity within rough-walled fractures under elevated effective stress through experimental results. Kulatilake et al. (2020) and Zhou et al. (2020) experimentally examined fluid flow through rough fractures under normal loading, revealing an initial rapid reduction in flow capacity at low closure stresses, followed by a gradual decline at higher stress levels. Deng et al. (2024) identified a threshold conductivity under high closure stress, where conductivity decreases by approximately eight orders of magnitude relative to initial values. Closure stress induces contact between micro-asperities within rough fracture voids, modifying flow boundaries. Zou et al. (2017) demonstrated that spatial variations in fracture surface roughness and the distribution of contacting micro-asperities generate complex flow phenomena, including channeling flow, transverse flow, and vortex flow. Xiong et al. (2018) also observed that contact areas increase flow path tortuosity, with tortuosity and associated eddies/backflow intensifying alongside rising contact ratios. Li et al. (2019) performed visualization experiments of rough fractures flow, and confirmed the formation of bypass flow around contacting micro-asperities. Li et al. (2021) conducted visualized core-flooding experiments of rough-walled fractures, and revealed that surface roughness significantly impaired fractures flow capacity, with only a minor fraction of the fracture void space functioning as effective flow channels. Zhang and Sanderson (1996) numerically simulated fluid flow through fractures under varying contact conditions, finding that excessive contact area impedes flow by reducing velocity. Li et al. (2022) observed through seepage experiments that increasing confining pressure elevates the proportion of contacting micro-asperities while progressively diminishing flow capacity; flow pathways initially deflect slightly around contacts but become increasingly tortuous as contact number and volume expand. However, contrasting findings exist: Wu et al. (2019) experimentally observed in Eagle Ford shale that fracture conductivity tended to increase with greater roughness. Similarly, Xia et al. (2024) reconstructed 3D single rough fracture models using morphology scanning technology and found rougher fractures exhibited greater flow capacity under identical stress. Evidently, the roughness morphology of fractures surface (Jansen et al., 2015), along with the spatial distribution of contact micro-asperities and non-contact regions under closure stress, critically governs fracture fluid flow (Rodríguez et al., 2024). Stress-induced fracture deformation and increased contact area enhance void space complexity (Chen et al., 2021), progressively intensifying fluid flow anisotropy and amplifying irregularity across macro- and micro-scales (Huang et al., 2025). To systematically characterize coupled fracture closure and conductivity degradation, researchers employ experimental and numerical methods to investigate both macroscopic flow behavior and microscopic characteristics within stressed rough fractures (Yang et al., 2024).

Nevertheless, the influence of closure stress on fracture geometry is inherently complex and multifaceted. This complexity impedes the isolation of individual effects, such as rough surface morphology or other geometric parameters, on the hydrodynamic characteristics of fractures (Cunningham et al., 2020). It is even more challenging to capture the regulatory mechanisms of multi-scale morphology on internal fluid flow within rough-walled fractures. Consequently, the influence of dynamically evolving roughness morphology on the coupled evolution characteristics of fracture deformation and fluid flow remains incompletely understood.

During hydraulic fracturing in shale oil and gas reservoirs, numerous self-propping fractures are generated. These fractures constitute critical pathways for subsurface hydrocarbon flow. As hydrocarbon extraction proceeds and formation pressure subsequently decreases, the effective stress acting upon these fractures progressively increases. This dynamic triggers a coupled evolution of stress-induced deformation and hydrodynamics properties in rough-walled fractures. By precisely controlling fracture surface roughness morphology and isolating individual geometric features, the macro-scale governing effects and micro-scale influence mechanisms of multi-scale roughness on self-propping fracture conductivity can be explicitly elucidated. This study employs a numerical approach to obtain fractures aperture distributions with controllable rough surface morphology. We systematically investigate the influence of roughness characteristics on the coupled mechanical-hydraulic evolution in self-propping fractures, analyze how micro-scale morphological variations govern macroscopic flow capacity, and ultimately elucidate the formation and evolution mechanisms of conductivity in self-propping fractures.

2. Numerical methodology

2.1. Model description

Fractal theory was applied to synthetically generate rough-walled fractures with self-affine roughness characteristics, precisely capturing their aperture properties. These synthetic fractures serve as the foundation for subsequent coupled mechanical-hydraulic simulations. The mechanical deformation model for rough-walled fractures (Hopkins, 2000; Pyrak-Nolte and Morris, 2000) is illustrated in Fig. 1(a), The physical model employs a cylindrical grid system. Based on the original fracture aperture distribution, the computational domain has geometric dimensions of 178 × 38 mm. The model configuration comprises two half-spaces representing fracture-surfaced bedrock and uniformly distributed cylindrical micro-asperities that characterize fracture surface roughness. The heights of micro-asperities are primarily determined by the fracture aperture and the relative positions of the bedrock. The model formulation assumes that: (1) mechanical interactions between discrete cylindrical micro-asperities and between the half-spaces are negligible, enabling linear superposition of deformation increments; (2) both the half-spaces and micro-asperities behave as ideal elastoplastic materials that obey the associated flow rule. The flow model in rough-walled fractures (Klimczak et al., 2010; Zhang and Sanderson, 1996) is illustrated in Fig. 1(b), the physical model employs a rectangular prism grid system with square cross-sections. Following the fractures aperture distribution after deformation, the computational model domain also features geometric dimensions of 178 × 38 mm. The model system is configured for horizontal flow, and the gravitational effects are neglected during simulations. Assuming the conductivity of fractures significantly exceeds that of the rock matrix, fluid is injected at a constant flow rate along the fracture length (*X*-axis direction).

2.2. Rough-walled fracture generation

The FBM method demonstrates robust adaptability for constructing geometrically heterogeneous structures of rough-walled fracture apertures (Mandelbrot and Van, 1968). By leveraging the FFT algorithm, we synthesize the initial aperture distribution of rough-walled fractures endowed with FBM characteristics (Wu et al., 2024; Pentland, 2009). The corresponding spectral density function conforms to the following mathematical representation:

$$S_{\mathrm{V}}(f) \propto \frac{1}{f^{2H+1}}. \tag{1}$$

where, $S_{\mathrm{V}}(f)$ is the spectral density function, f is the frequency components, H is the Hurst exponent, $0 < H < 1$, for two-dimensional rough-walled fractures, the Hurst exponent H and fractal dimension F_{D} satisfy a relationship of $F_{\mathrm{D}} = 3-H$.

Since the spectral density lies within the *u*-*v* plane, it exhibits statistical isotropy in directional components. For two-dimensional systems, this implies:

$$f = \sqrt{f_i^2 + f_j^2}. \tag{2}$$

where f_i and f_j denote the frequency components in the *u*- and *v*-directions, respectively, the following relationship holds:

$$S_{\mathrm{V}}(f) \propto \frac{1}{\left(f_i^2 + f_j^2\right)^{H+1}} \propto \frac{1}{\left(f_i^2 + f_j^2\right)^{4-F_{\mathrm{D}}}}. \tag{3}$$

By employing a random number generator to synthesize a white noise sequence W and subsequently filtering it through a shaped filter defined by the transfer function $T(f)$, a targeted power spectral density for the fractures aperture distribution function can be synthesized, where the spatial scaling properties are governed by the Hurst exponent H.

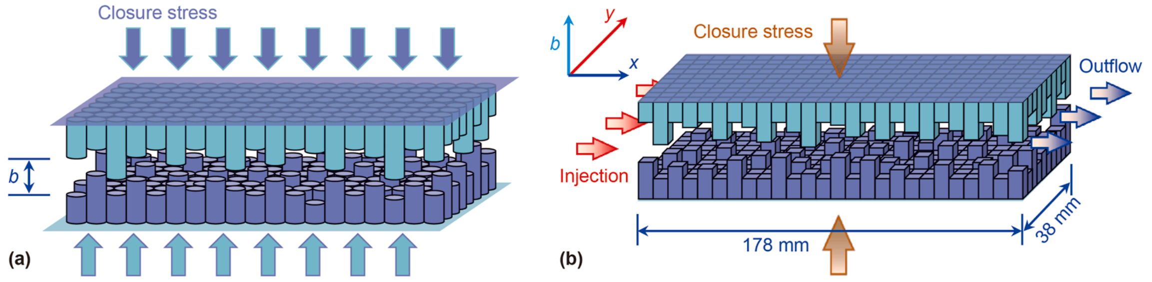

Fig. 1. Schematic diagram of the mechanical-hydraulic coupling model for self-propping fractures.

$$S_{\mathrm{V}}(f) \propto |T(f)|^2 S_{\mathrm{W}}(f). \tag{4}$$

The spectral density of white noise, $S_{\mathrm{W}}(f)$, is a constant, and the following relationship holds:

$$S_{\mathrm{V}}(f) \propto |T(f)|^2. \tag{5}$$

Therefore, the transfer function of the shaped filter is given by:

$$T(f) \propto \frac{1}{\left(f_i^2 + f_j^2\right)^{(H+1)/2}}. \tag{6}$$

The workflow proceeds as follows: First, obtaining the amplitude and phase spectra for all frequency pairs (f_i, f_j). Subsequently, determining the value of the Hurst exponent H and evaluating the transfer function $T(f_{i,\,j}) = a_{ij}$ by using Eq. (6). Finally, applying the inverse Fourier transform by using the formulation below to derive the corresponding fractures aperture distribution, can be expressed as follows.

$$f(x,y) = \sum_{j=0}^{N-1} \sum_{i=0}^{M-1} a_{ij} \mathrm{e}^{2\pi i(ix+jy)}. \tag{7}$$

where, $f(x, y)$ denotes the original fracture aperture distribution function; M and N represent the number of discretized grid cells along the X- and Y- directions.

2.3. Mechanical deformation model

Under closure stress, the total deformation at any location within a rough fracture comprises both micro-asperities and corresponding half-spaces (Petrovitch et al., 2014; Zeng and Zhou, 2025). The geometric constraints dictates that the algebraic sum of the initial half-space separation distance D and the cumulative half-spaces deformation at the location of micro-asperity i remains equivalent to compressed length of the micro-asperities after deformation, expressed by Eq. (8).

$$D + W_i = L_i^0 - \Delta L_i. \tag{8}$$

The total deformation of the half-space at a radial distance r from the micro-asperities center, induced by calculating the forces acting on individual micro-asperities via the superposition method, can be expressed as:

$$W_i = f_i \frac{8\left(1-\nu^2\right)}{\pi^2 E a} \frac{\int_{D_i} I\left(\frac{r}{a}\right) r \mathrm{d}\theta \mathrm{d}r}{\pi a^2} = f_i \frac{3.4\left(1-\nu^2\right)}{\pi E a}. \tag{9}$$

$$\begin{cases} I\left(\dfrac{r}{a}\right) = \displaystyle\int_0^{\frac{\pi}{2}} \sqrt{1-\left(a^2/r^2\right)\sin^2\theta}\,\mathrm{d}\theta - \left(1-\frac{a^2}{r^2}\right) \\ \qquad \displaystyle\int_0^{\frac{\pi}{2}} \frac{\mathrm{d}\theta}{\sqrt{1-\left(a^2/r^2\right)\sin^2\theta}} \quad r > a \\ I\left(\dfrac{r}{a}\right) = \displaystyle\int_0^{\frac{\pi}{2}} \sqrt{1-\left(a^2/r^2\right)\sin^2\theta}\,\mathrm{d}\theta \quad r < a \end{cases}. \tag{10}$$

During the plastic deformation of micro-asperities, contact stress remains constant at the yield strength of the formation rocks, while elastic deformation is governed by Hooke's law for displacement calculation, expressed as:

$$\Delta L_i = f_i \frac{L_i^0}{E\pi a^2}. \tag{11}$$

Upon achieving mechanical equilibrium, the closure stress and contact stress of the micro-asperities must satisfy the equilibrium criterion, expressed as:

$$\sigma_{\mathrm{c}} = \sum_{i=1}^{n} f_i \Big/ A. \tag{12}$$

The contact stresses of micro-asperities in three distinct deformation regimes: elastic contact, plastic contact, and non-contacting regime, are respectively expressed as follows:

$$f_i = \begin{cases} d - b_0 \Big/ \left(\dfrac{3.4\left(1-\nu^2\right)}{\pi E a} + \dfrac{L_i^0}{\pi E a^2}\right) & \text{Elastic deformation} \\ \pi \sigma_{\max} a^2 \quad \text{Plastic deformation} \\ 0 \quad \text{No contact} \end{cases}. \tag{13}$$

where D is the initial distance between the half-space, mm; W_i is the total deformation at the location of micro-asperity i, mm; L_i^0 is the height of micro-asperities, mm; E is the Young's modulus, MPa; ν is the Poisson's ratio, dimensionless; ΔL_i is the deformation of micro-asperities, mm; a is the radius of micro-asperities, mm; f_i is the force acting on micro-asperities, N; r is the distance from a certain point to the center of a certain micro-asperities, mm; D_i is the integral region; A is the projected area of the fracture surface, m^2; σ_{c} is the closure stress, MPa; d is the distance of mutual approach in half-space under closure stress, mm; $\sigma_{\max}$ is the compressive strength of the formation rocks, MPa.

2.4. Fluid flow and conductivity model

The fluid flow within fractures is mathematically characterized as a steady-state single-phase incompressible and isothermal fluid flow, and the Navier-Stokes equations can be written as the following vector forms respectively (Baghbanan et al., 2008; Wang et al., 2024):

$$\nabla \cdot u = 0, \tag{14}$$

$$\rho(u\nabla)u = \mu\nabla^2 u - \nabla P, \tag{15}$$

Assuming that fluid flow within the fractures is constant laminar and inertial forces within the fluid are negligible compared to viscous forces and pressure. And for Darcy flow, assuming that the single fracture consists of two smooth parallel plates, the local cubic law (Koyama et al., 2008; Lee et al., 2014), which describes a linear relationship between flow rate and pressure gradient, can be obtained:

$$u = -\frac{b^3}{12\mu}\nabla P, \tag{16}$$

Based on the material balance equation, the continuity equation within these fractures is expressed in Eq. (17).

Table 1
The requisite rock mechanical and hydraulic parameters.

Parameter	Value	Unit
Young's modulus	40.91	GPa
Poisson's ratio	0.18	Dimensionless
Compressive strength	320	MPa
Fractal dimension	2.1, 2.3, 2.5, 2.7, 2.9	Dimensionless
Fluid viscosity	1.0 (fresh water)	mPa·s
Flow rate	10.0	mL/min
Closure stress	10, 20, 30, 40, 50, 60, 70	MPa
Random seed	24	Dimensionless
Minimum fracture aperture	0	mm
Maximum fracture aperture	5	mm

$$\frac{1}{12\mu}\frac{\partial}{\partial x}\left(b^3\frac{\partial P}{\partial x}\right)+\frac{1}{12\mu}\frac{\partial}{\partial y}\left(b^3\frac{\partial P}{\partial y}\right)=0. \tag{17}$$

where, u represents the fluid flow velocity tensor, m/s; b represents the fracture width, mm; P represents the fluid pressure inside the fractures, Pa; μ represents the fluid viscosity, Pa·s.

The Neumann boundary was imposed on the two boundaries except the inlet and outlet, expressed as follows:

$$\left.\frac{\partial P}{\partial x}\right|_{y=0}=0 \quad \forall x, t>0, \tag{18}$$

$$\left.\frac{\partial P}{\partial y}\right|_{y=H}=0 \quad \forall x, t>0, \tag{19}$$

The Dirchlet boundary is applied at the outlet, expressed:

$$P(L,H)=P_{\mathrm{e}} \quad \forall y, t>0. \tag{20}$$

Darcy's law is applied to establish the functional relationship between fracture conductivity and the pressure difference between inlet and outlet (Wei et al., 2022), where conductivity is defined as:

$$k_{\mathrm{f}}w_{\mathrm{f}}=0.01667\times\frac{Q\mu L_{\mathrm{f}}}{H_{\mathrm{f}}\left(P_{\mathrm{inj}}-P_{\mathrm{e}}\right)}. \tag{21}$$

where, $k_{\mathrm{f}}w_{\mathrm{f}}$ is fracture conductivity, μm^2·cm; H_{f} is cross-sectional width of the flow channel, cm; L_{f} is fracture length, cm; Q is flow velocity, mL/min; P_{inj} is injection pressure at the injection end, kPa; P_{e} is boundary pressure at outflow end, kPa.

3. Model solution and validation

3.1. Model solution

Taking the Cambrian Qiongzhusi Formation shale in the Sichuan Basin as a case study, and based on the rough-walled fracture generation method established herein, along with the corresponding mechanical deformation and flow models, we simulated the evolution of closure and fluid flow within self-propping fractures within the shale reservoir under varying closure stresses. The requisite rock mechanical and hydraulic parameters are provided in Table 1. Regarding the fractal dimension of rough-walled fractures, the majority of published papers report values typically within the range of $F_{\mathrm{D}}=2.0$ to 2.55 (Kong and Chen, 2018; Li et al., 2024). However, some experimental studies have demonstrated that the fractal dimension of rough-walled fractures can reach $F_{\mathrm{D}}=2.6$ or higher values (Lu et al., 2020, 2021), as shown in Fig. 2. Therefore, in common with some existing numerical simulation studies, this research adopts a relatively broad range of fractal dimension values to enhance the applicability and coverage of the study's conclusions. The injection rate was determined in accordance with the Reynolds number calculation method described in previous literature (Cheng et al., 2017; Cheng et al., 2024), thereby ensuring the maintenance of laminar flow conditions throughout all numerical simulations.

The mechanical deformation of rough-walled fractures is discretized using the finite difference method and solved numerically via the Newton-Raphson iterative method. Fluid flow model is discretized using the five-point central difference scheme and solved numerically via the Gauss-Seidel iterative method. The computational workflow for numerical simulation of the coupled system is illustrated in Fig. 3. Within this framework, geometric deformation of rough-walled fractures under closure stress inherently modifies the boundaries of flow pathways (Xia et al., 2024). When computing flow fields within partially closed fractures, contact regions and fluid domains are modeled as a unified computational domain for coupled solution. Critically, at the beginning of each solution iteration, velocity within contact regions is explicitly set to zero. This enforces no-slip boundary

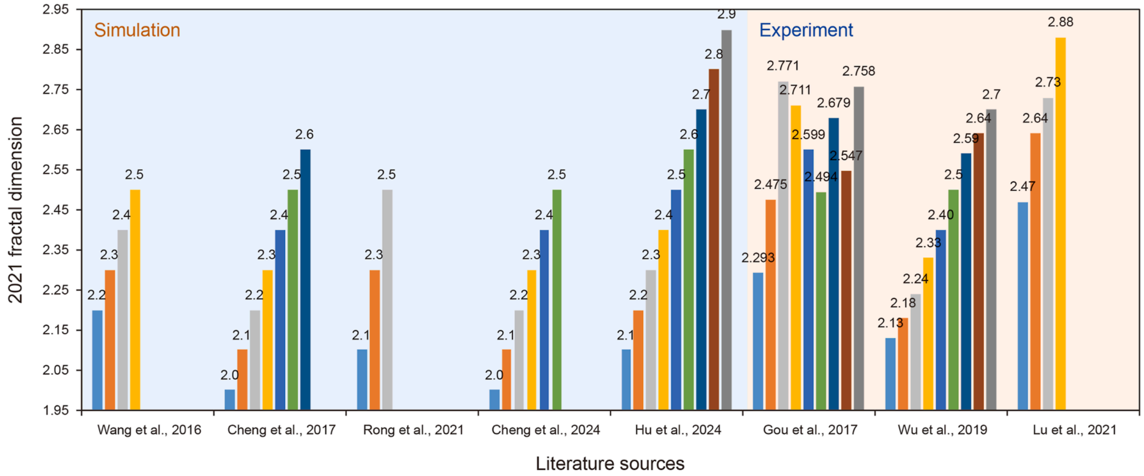

Fig. 2. Analysis of fractal dimension assignment for rough fractures in the literatures.

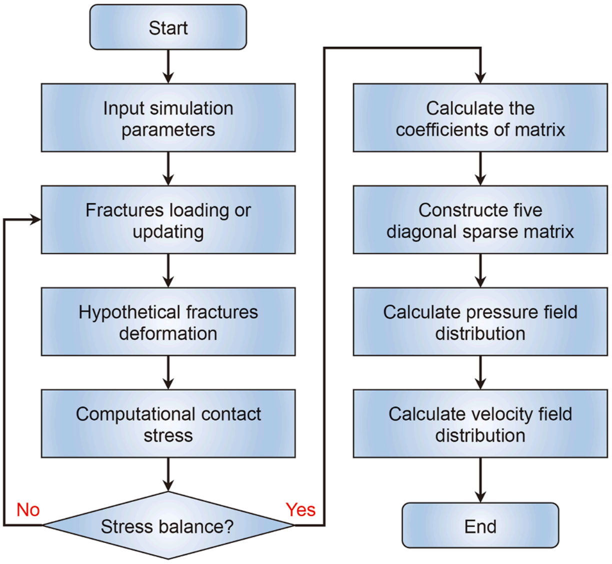

Fig. 3. Flowchart of mechanical-hydraulic coupled model solution.

conditions, ensuring contact nodes impose zero-velocity constraints on adjacent fluid nodes.

3.2. Model validation

To ensure numerical simulation accuracy was not unduly affected by mesh resolution, fluid flow simulations within rough-walled fractures under closure stress were performed using meshes of varying geometric resolution, as illustrated in Fig. 4. The results indicate that as the mesh size decreases, the number of elements increases exponentially, substantially elevating computational demands and simulation duration. When the mesh size is reduced to 1 mm, the calculated fracture conductivity converges to a stable value. Consequently, a uniform mesh size of 1 mm was implemented for all subsequent simulations in this study. Furthermore, to prevent the meshing process itself from altering the local fractal dimension of the fracture, the identical 1 mm resolution was employed during the numerical generation of the rough-walled fracture surfaces.

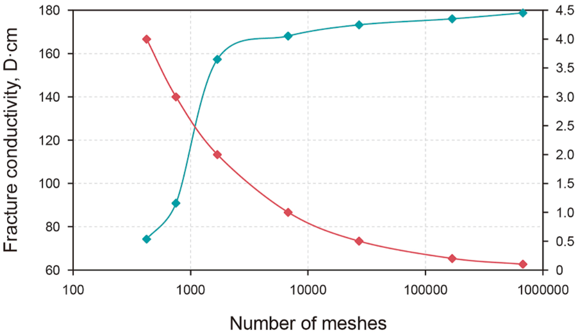

Fig. 4. Analysis diagram of mesh size independence of the simulation (F_D = 2.7, closure stress = 10).

Results from experimental tests on the mechanical deformation of rough-walled fractures and their conductivity under closure stress, reported in previously published researches, were used to validate the model presented in this study. These comparative results are shown in Fig. 5. The mechanical-deformation calculation results for rough-walled fractures exhibit typical stress-deformation curve behavior (Guan et al., 2012). Both the shape of the curve depicting the variation of deformation with closure stress and the absolute magnitude of the deformation show good agreement with previously published studies (Gou, 2017; Lu et al., 2019, 2020; Jiang et al., 2020; Chen, 2022). This demonstrates the reliability of the simulation results obtained from the mechanical-deformation model for rough-walled fractures. The calculated conductivity curves for rough fractures under closure stress exhibit an exponential decline trend consistent with experimentally measured results reported in the literature (Gou, 2017; Wu, 2019; Lai et al., 2019; Lu et al., 2019; Chen et al., 2021; Chen, 2022; Aliu et al., 2022). Furthermore, the calculated conductivity magnitudes remain within the same order of magnitude as these experimental measurements. This consistency demonstrates the reliability of the fracture conductivity calculations under closure stress.

4. Results and discussion

4.1. Aperture of rough-walled fractures

The rough morphology represents one of the most prominent characteristics and concurrently serves as a critical factor governing the mechanical behavior and hydraulic properties of rock fractures. Five distinct fracture sets with fractal dimensions of 2.1, 2.3, 2.5, 2.7, and 2.9 were numerically generated, as illustrated in Fig. 6. Statistically, all fracture apertures exhibit distributions within the range of 0–5 mm, with mean values (M) of approximately 2.5 mm and standard deviations (σ_{StDev}) around 0.7. The original aperture distributions conform closely adhere to a normal distribution, demonstrating negligible differences across fractures with varying fractal dimensions and maintaining high consistency. From the perspective of aperture distribution, fractures with lower

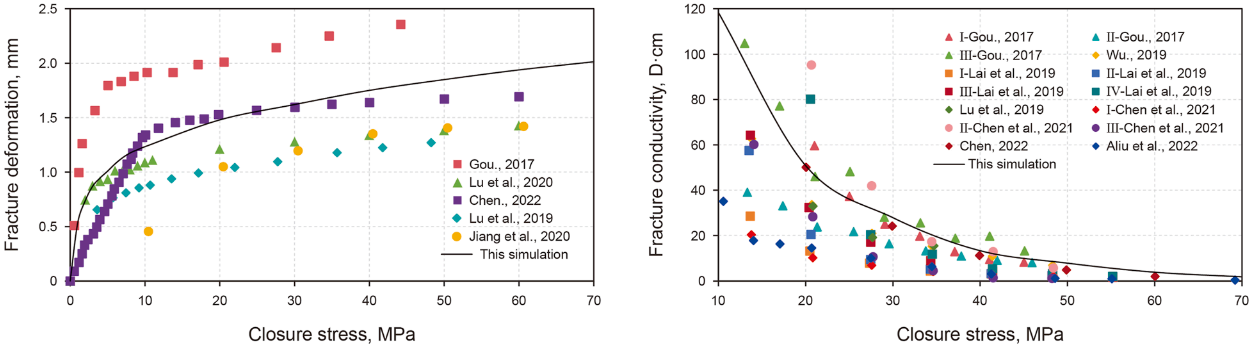

Fig. 5. Comparison between numerical simulation results and experimental test results (F_D = 2.1).

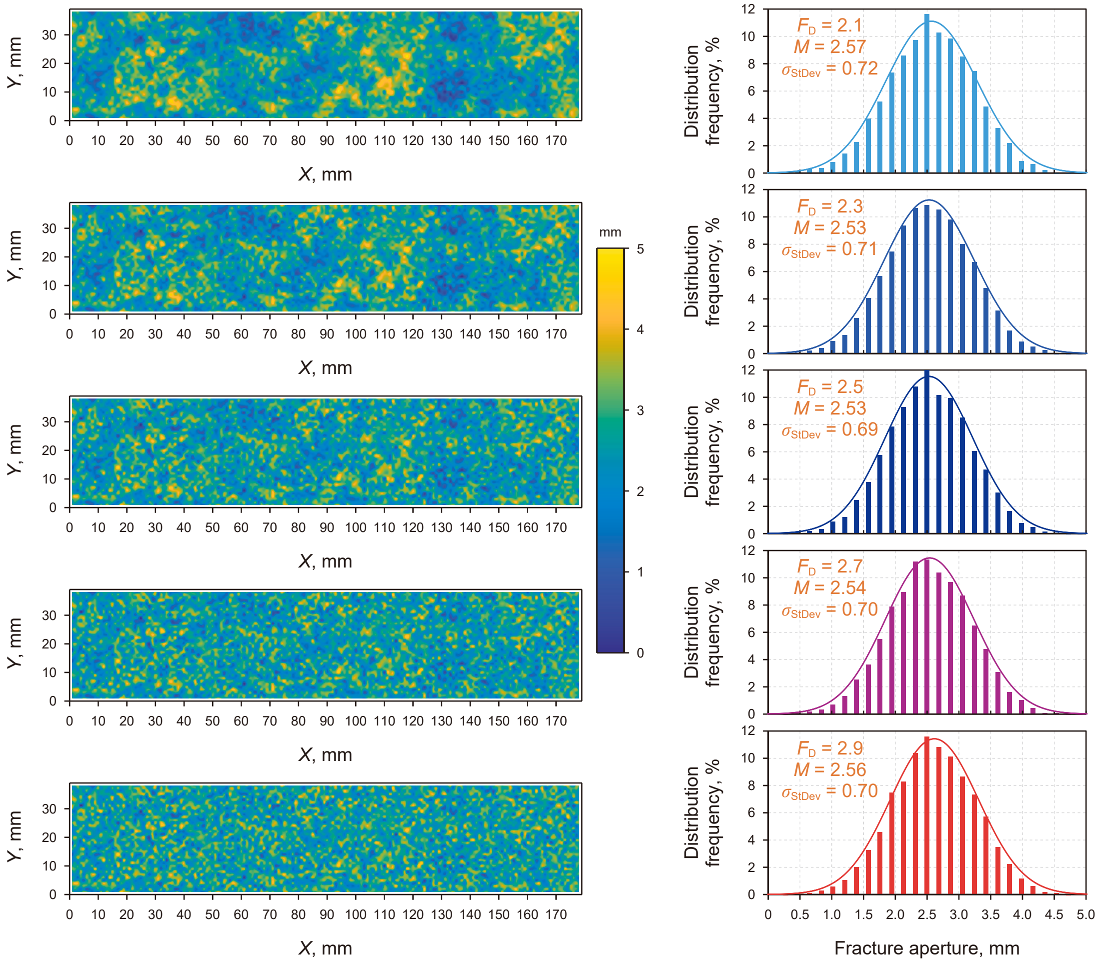

Fig. 6. Original fractures aperture and statistical characteristics with varied fractal dimensions.

fractal dimension exhibit more pronounced clustering of both larger and smaller aperture regions. This distinct clustering progressively diminishes with increasing fractal dimension, resulting in a more dispersed and homogeneous distribution of aperture sizes throughout the fractures. A fractures aperture profile curve was constructed along the X-axis direction at $Y = 19$ mm through data path acquisition, as illustrated in Fig. 7. Fractures with different fractal dimensions exhibit fundamentally consistent undulation trends in their aperture profiles. However, fractures with lower fractal dimensions demonstrate reduced amplitude fluctuations in aperture variations, characterized by smoother transitions between adjacent peaks and troughs. This phenomenon arises from the spatial concentration of wider and narrower aperture zones. Conversely, fractures with higher fractal dimensions display more pronounced fluctuation amplitudes, manifesting as large-amplitude, short-wavelength variations

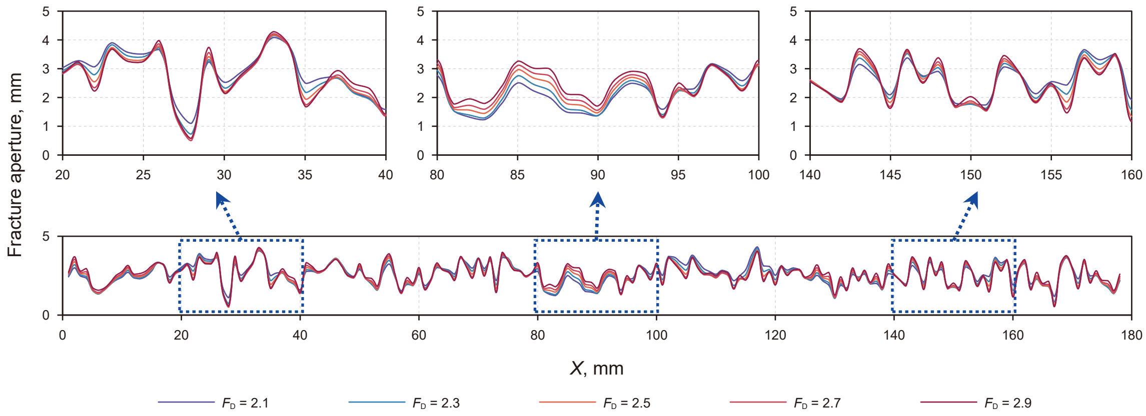

Fig. 7. The cross-sectional profile curves of fractures aperture with varying fractal dimensions.

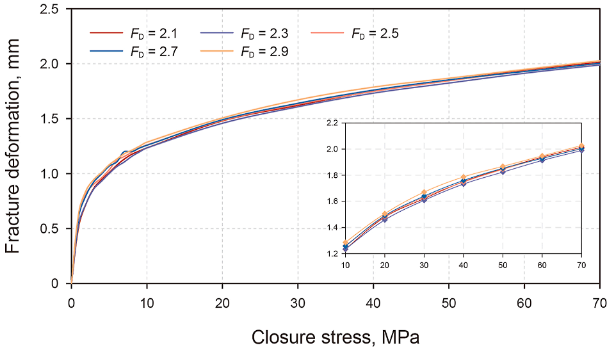

Fig. 8. The deformation characteristics in fractures with distinct fractal dimensions subjected to differential closure stress.

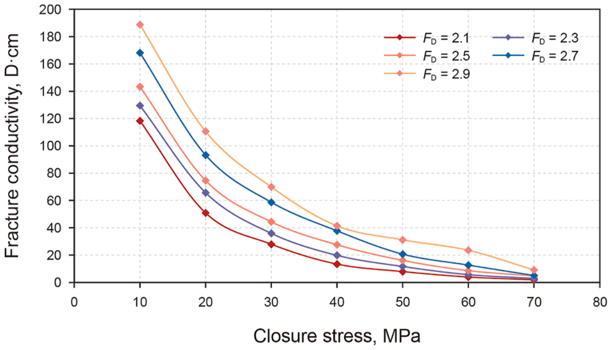

Fig. 9. The fracture conductivity with distinct fractal dimensions subjected to differential closure stress.

between peak and troughs. This intensified roughness stems from the discrete spatial arrangement of wide and narrow aperture regions, where alternating high and low aperture zones create abrupt interfacial transitions along the fracture interfaces.

4.2. *Stress-dependent flow attenuation characteristics in rough-walled fractures*

Computational results for fracture deformation and conductivity are systematically presented in Figs. 8 and 9, respectively. We observe that fractures with distinct fractal dimensions exhibit highly consistent deformation magnitudes and patterns under closure stress. Specifically, rapid compression with large deformation occurs in the low-stress regime (10–40 MPa), whereas gradual compression with small deformation occurs in the high-stress regime (40–70 MPa). The maximum discrepancy in deformation magnitudes across different closure stress levels peaks at a mere 3.77%. Similarly, fracture conductivity progressively declines with increasing closure stress, showing marked reduction in the low-stress regime (10–40 MPa) and attenuated decline in high-stress regime (40–70 MPa). At 40 MPa, conductivity decreases to 7.7%–16.5% of its value at 10 MPa. When stress reaches 70 MPa, conductivity further decline to 1.6%–4.8% of the 10 MPa reference value. Nevertheless, this residual conductivity still exceeds the matrix permeability of formation rocks (Zhou et al., 2019). Over an identical 30 MPa stress interval, deformation in the low-stress regime is 1.9–2.1 times greater than in the high-stress regime, while conductivity degradation shows a more pronounced disparity of 4.6–9.1 times. This indicates strong coupling between fracture deformation and conductivity degradation: significant aperture compression triggers rapid conductivity decline, whereas

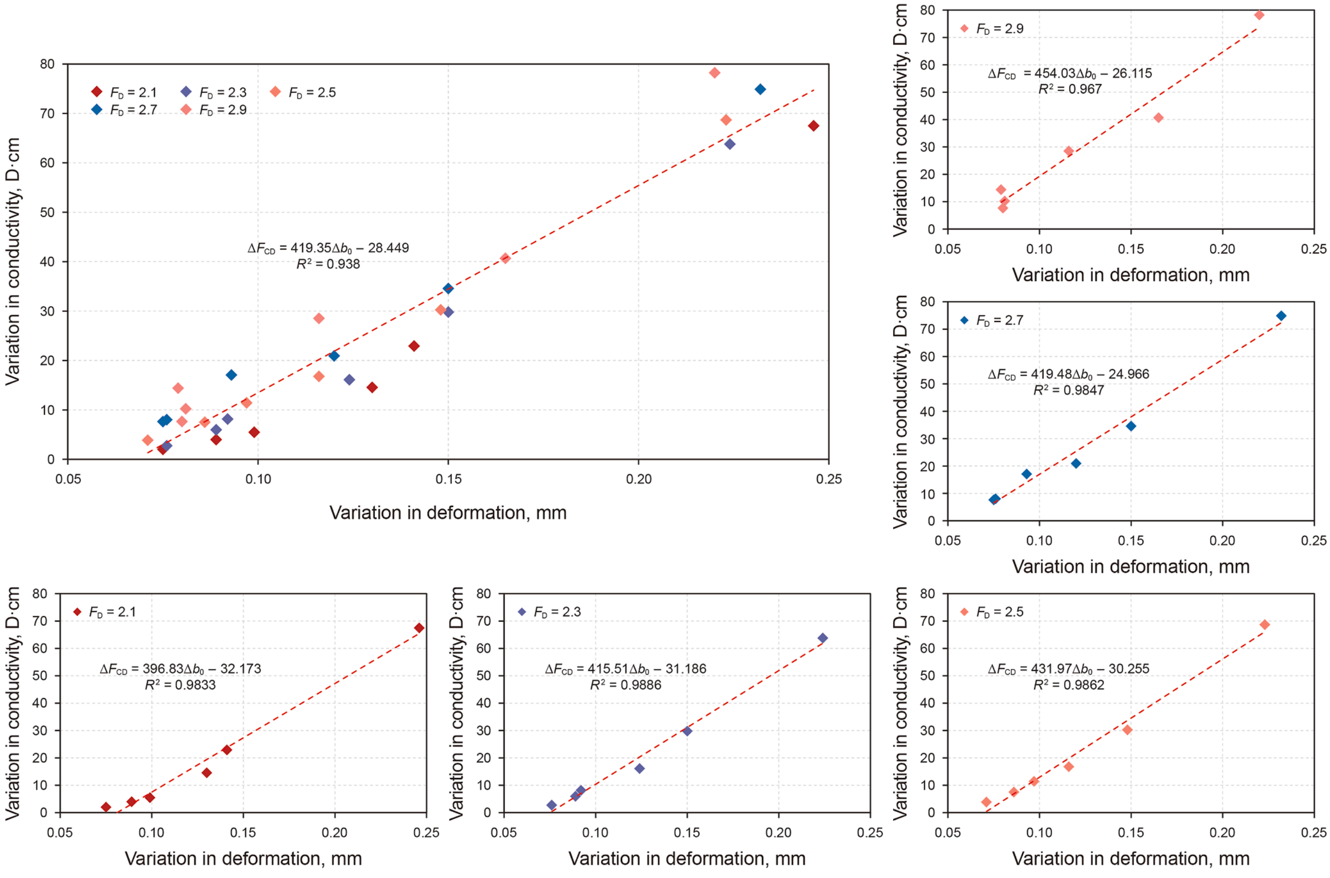

Fig. 10. Correlation between the fracture deformation and the corresponding conductivity attenuation.

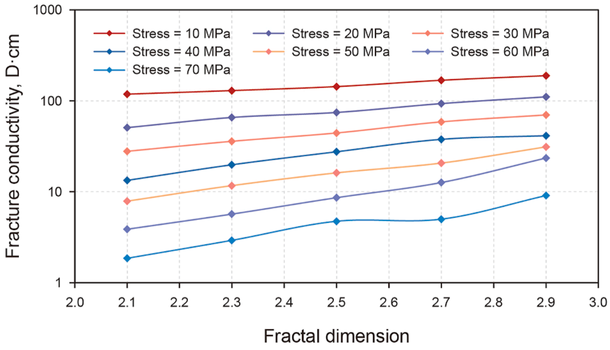

Fig. 11. The variation of fracture conductivity with fractal dimensions.

minor aperture reduction corresponds to gradual deterioration. As shown in Fig. 10, changes in fracture deformation (Δb_0) and conductivity attenuation (ΔF_{CD}) exhibit a clear linear positive correlation per 10 MPa stress increment, as evidenced by the coefficient of determination (R^2) greater than 0.938. This confirms that fracture width reduction under closure stress directly drives the concurrent decrease in conductivity.

4.3. *Effect of fractal dimension on conductivity in rough-walled fractures*

Based on simulation results, the influence of fractal dimensions on the conductivity of self-propping fractures was further analyzed, as illustrated in Fig. 11. The results demonstrate that fracture conductivity increases progressively with rising fractal dimension, exhibiting a linear positive correlation. This indicates that greater fracture roughness corresponds to superior conductivity under closure stress. Notably, this observation contrasts with conventional research perspectives associating increased roughness with elevated flow resistance (Tzelepis et al., 2015; Xiao and Zhao, 2019; Hu et al., 2024; Kong and Chen, 2018). Although higher fractal dimension introduces more complex structural features that could impede flow, the application of closure stress induces a significant restructuring of flow channels within the fractures space. Crucially, these morphological characteristics enhances the stress disturbance resistance of the fracture architecture. Compressive stress loading maintains primary flow pathways integrity through mechanical stabilization. This counterintuitive phenomenon fundamentally arises from the stress-induced geometric optimization mechanism. The synergistic interaction between fractal roughness and stress-mediated deformation promotes advantageous reconfiguration of flow conduits rather than merely exerting obstructive effects.

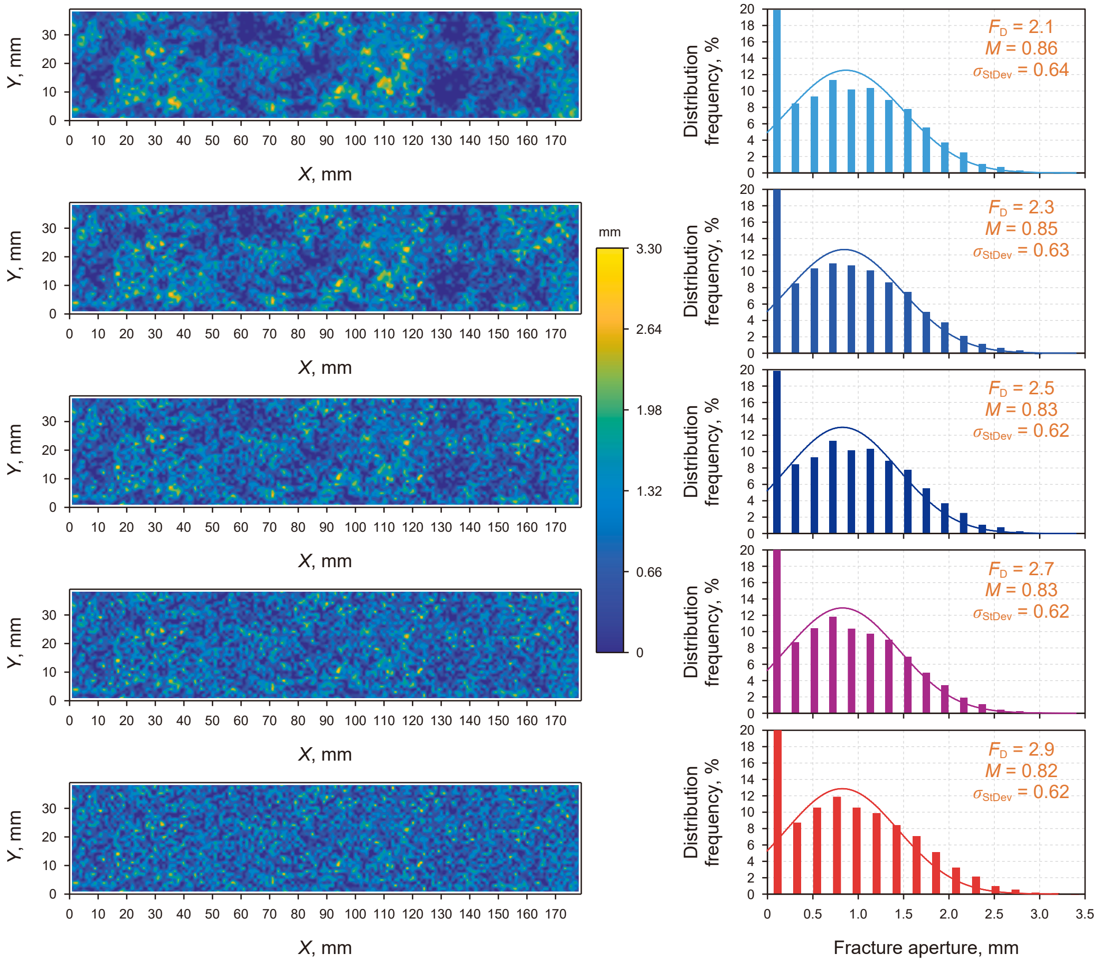

Fig. 12. Fractures aperture and statistical characteristics with varied fractal dimensions under closure stress of 40 MPa.

As a representative case under 40 MPa closure stress, the aperture distributions of fractures with varying fractal dimensions were systematically analyzed following stress-induced deformation, as illustrated in Fig. 12. Statistically, the five fracture sets exhibit residual aperture distributions ranging from 0 to 3.3 mm, with mean values approximately 0.8 mm and standard deviations of about 0.6, demonstrating favorable consistency in their distribution patterns. Regarding aperture distribution, fractures with lower fractal dimensions exhibit a more concentrated distribution of contact micro-asperities within the fractures, characterized by dense clustering. As the fractal dimension increases, this clustered pattern gradually diminishes, and the contact micro-asperities become progressively dispersed throughout the entire fractures. This behavior aligns closely with the distribution of narrower aperture regions in the original fracture width distribution. This alignment occurs because regions with smaller apertures preferentially form effective supporting contacts during compressive deformation to resist closure stress. Through precise control of the initial fracture width distribution in rough-walled fractures, all groups exhibit highly consistent average fracture widths and width distributions before and after closure stress loading and deformation, as intended. This demonstrates that the observed variations are primarily governed by fractal dimension, with most extraneous factors effectively eliminated.

The geometric dimensions and spatial distributions of “cluster-like” and “discrete-like” contact micro-asperities within fractures constitute critical factors influencing the flow capacity variation of self-propping fractures across fractal dimensions. As Fig. 13(a) illustrates, these contact micro-asperities intensify the fluid pressure drop. Both the number of micro-asperities along the flow path and the size of high-density “cluster-like” regions correlate positively with the magnitude of this pressure drop. Furthermore, larger high-density “cluster-like” regions significantly constrict the fracture flow channel area, forming distinct “throat-like” structures. Fig. 13(b) presents flow pressure distribution curves derived from X-axis data paths at $Y = 19$ mm. Fractures with fractal dimensions $F_D = 2.1$ and $F_D = 2.3$ exhibit a characteristic “stepwise pressure decline” pattern. At three primary “throat-like” structures, significant pressure buildup occurs upstream, resulting in a gradual pressure decrease, while a noticeable sharp pressure drop is observed immediately downstream of each constriction. This phenomenon results from flow impedance geometric constrictions, where localized pressure accumulation precedes sudden energy dissipation across structural discontinuities. Across these three throats, the cumulative pressure loss relative to the injection pressure is 15.18%, 19.36%, and 47.42% for $F_D = 2.1$, and 11.20%, 23.40%, and 33.27% for $F_D = 2.3$. The throttling effect of these “throat-like” structures accounts for approximately 81.96%

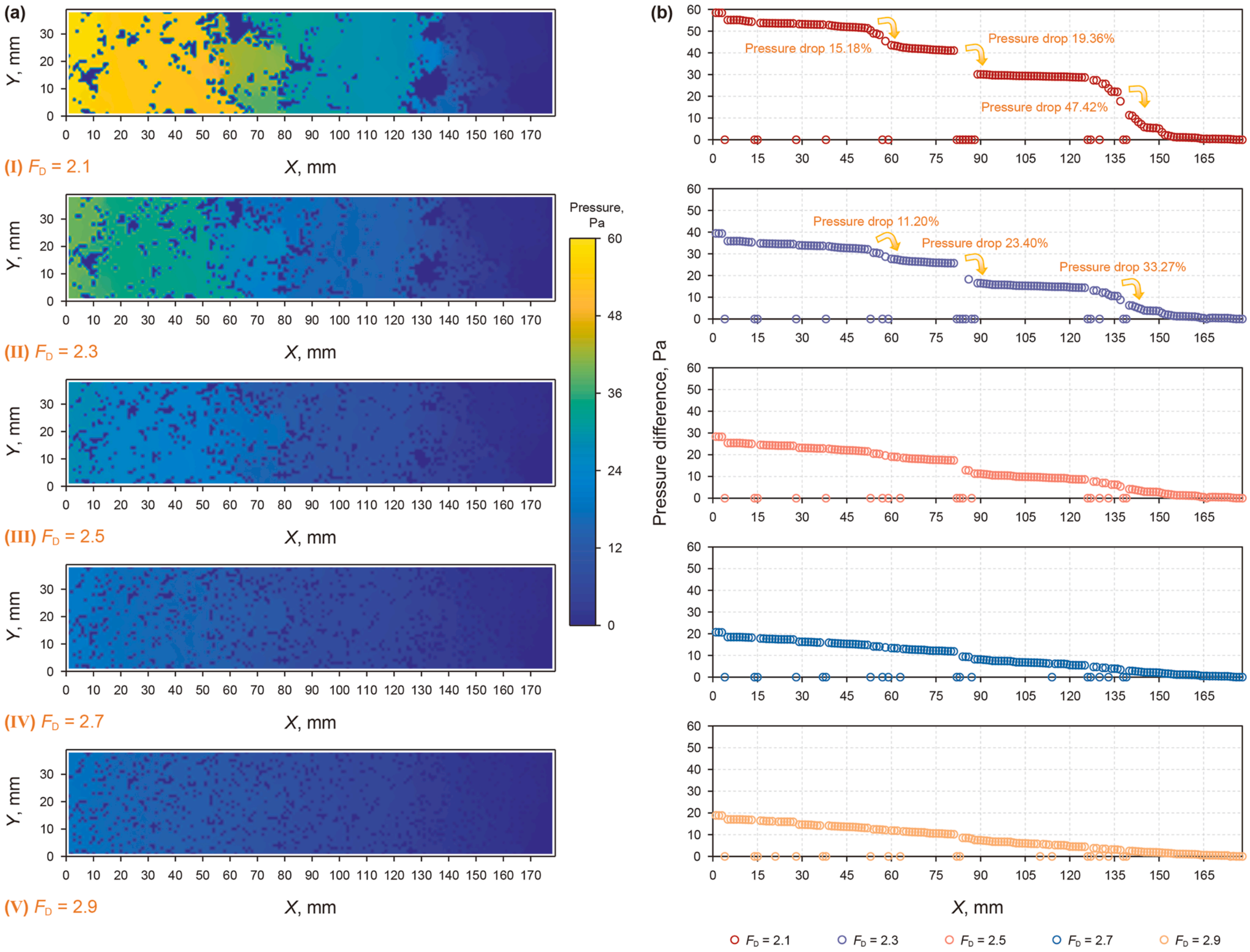

Fig. 13. The pressure field distribution characteristics in fractures with varying fractal dimensions under closure stress of 40 MPa.

($F_D = 2.1$) and 67.87% ($F_D = 2.3$) of the total pressure loss, establishing them as a dominant factor in flow pressure reduction and diminished fracture conductivity. In contrast, fractures with higher fractal dimensions ($F_D = 2.5$, 2.7, 2.9) display a linear pressure decline along their length. This behavior stems from the absence of pronounced "throat-like" structures. Consequently, flow dynamics are predominantly governed by microscale roughness variations. The lack of significant macroscopic flow channel differences amplifies the influence of microscopic heterogeneities on pressure propagation, resulting in the observed consistent linear pressure gradient.

The non-uniformly distributed rough surfaces of fractures perturb flow dynamics, resulting in a highly heterogeneous distribution of both magnitude and direction of flow velocities within them. The presence and localized aggregation of micro-asperities zones further exacerbate flow complexity, ultimately inducing flow channel reorganization and reconfiguration, as graphically demonstrated in Fig. 14. For fractures with fractal dimensions of $F_D = 2.1$ and $F_D = 2.3$, regions formed by high-density "cluster-like" contact micro-asperities significantly constrict flow pathways, resulting in a series of high-velocity flow regions. These high-velocity regions interconnect to constitute the primary flow channels through the fractures. Meanwhile, fluid flow outside these channels is largely suppressed, with most external fluid remaining stagnant or exhibiting negligible participation in the overall flow dynamics. The emergence of primary flow channels induces meandering of fluid pathways, increasing actual distance traveled through the fractures beyond the fractures length thereby elevating flow resistance. Furthermore, when fluids encounter smaller scales contact micro-asperities, flow bifurcation and directional reorientation occur, after circumventing these contact micro-asperities, the fluid re-converges, forming a "bypass flow" pattern. Conversely, interaction with larger-scale contact micro-asperities results in fluid movement dominated by geometric constraints of the contact zones, giving rise to specialized flow phenomena such as "transverse flow" and "reverse flow". These multi-scale flow modifications collectively contribute to a significant enhancement of fluid flow resistance within fractures. For fractures with fractal dimensions $F_D = 2.5$, $F_D = 2.7$, and $F_D = 2.9$, the aggregation of high-density "cluster-like" contact micro-asperities gradually weakens with increasing fractal dimensions. The fluid flow direction becomes predominantly aligned parallel to the fracture length direction, resulting in an actual flow path length nearly equivalent to the fracture length. Meanwhile, the "discrete-like" distribution of contact micro-asperities induces alterations in flow boundary conditions. This spatial configuration fragments, cuts, and disturbs the flow domain, predominantly generating "bypass flow" while significantly suppressing the occurrence of "diffusion flow" and "reverse flow". This hydrodynamics characteristic is manifested in relatively lower flow resistance through these fractures. Both the high-density "cluster-like" contact micro-asperities regions and the "throat-shaped" constriction structures constitute critical factors affecting the overall flow capacity of the fractures. These distinctive

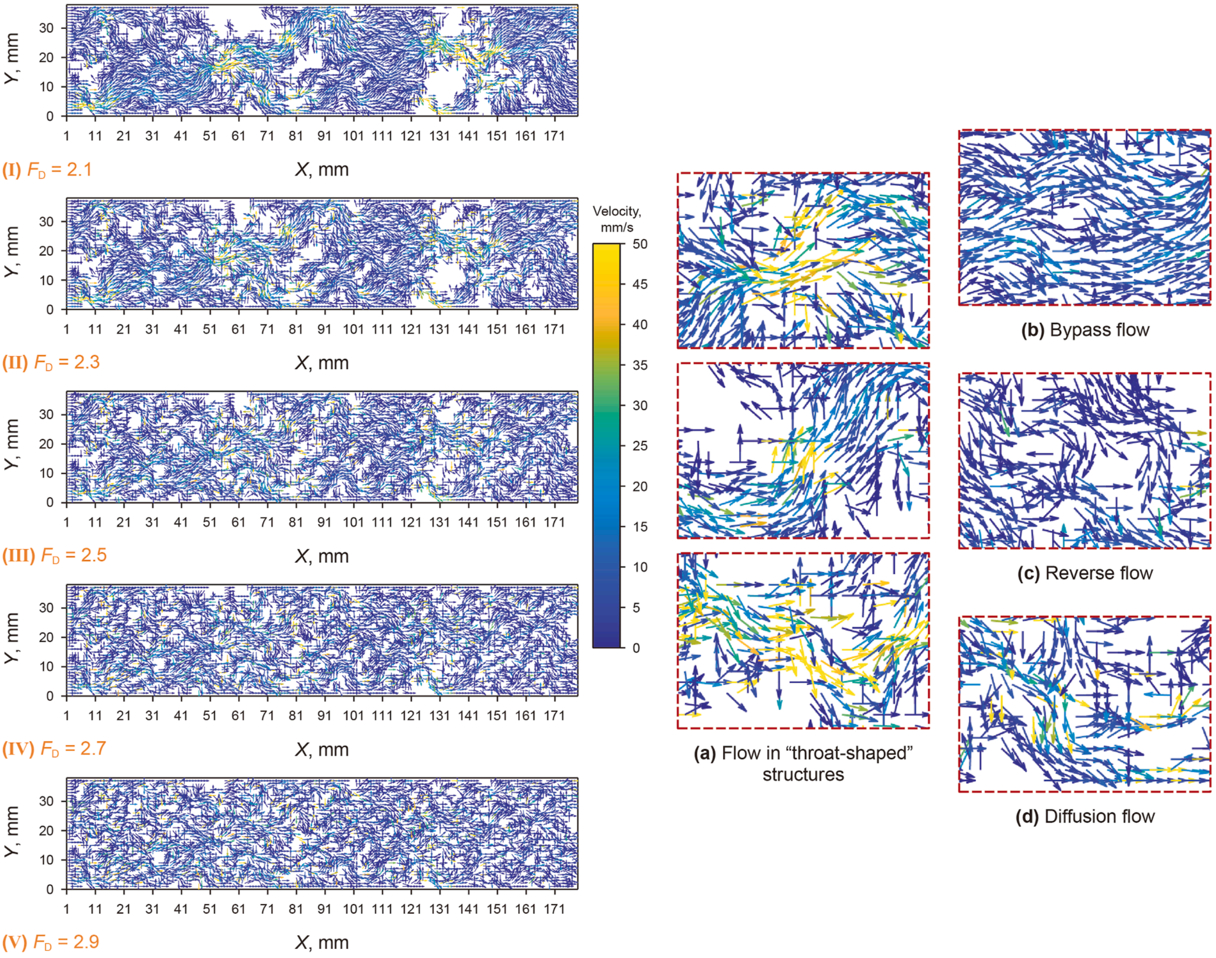

Fig. 14. The flow fields distribution characteristics in fractures with varying fractal dimensions under closure stress of 40 MPa.

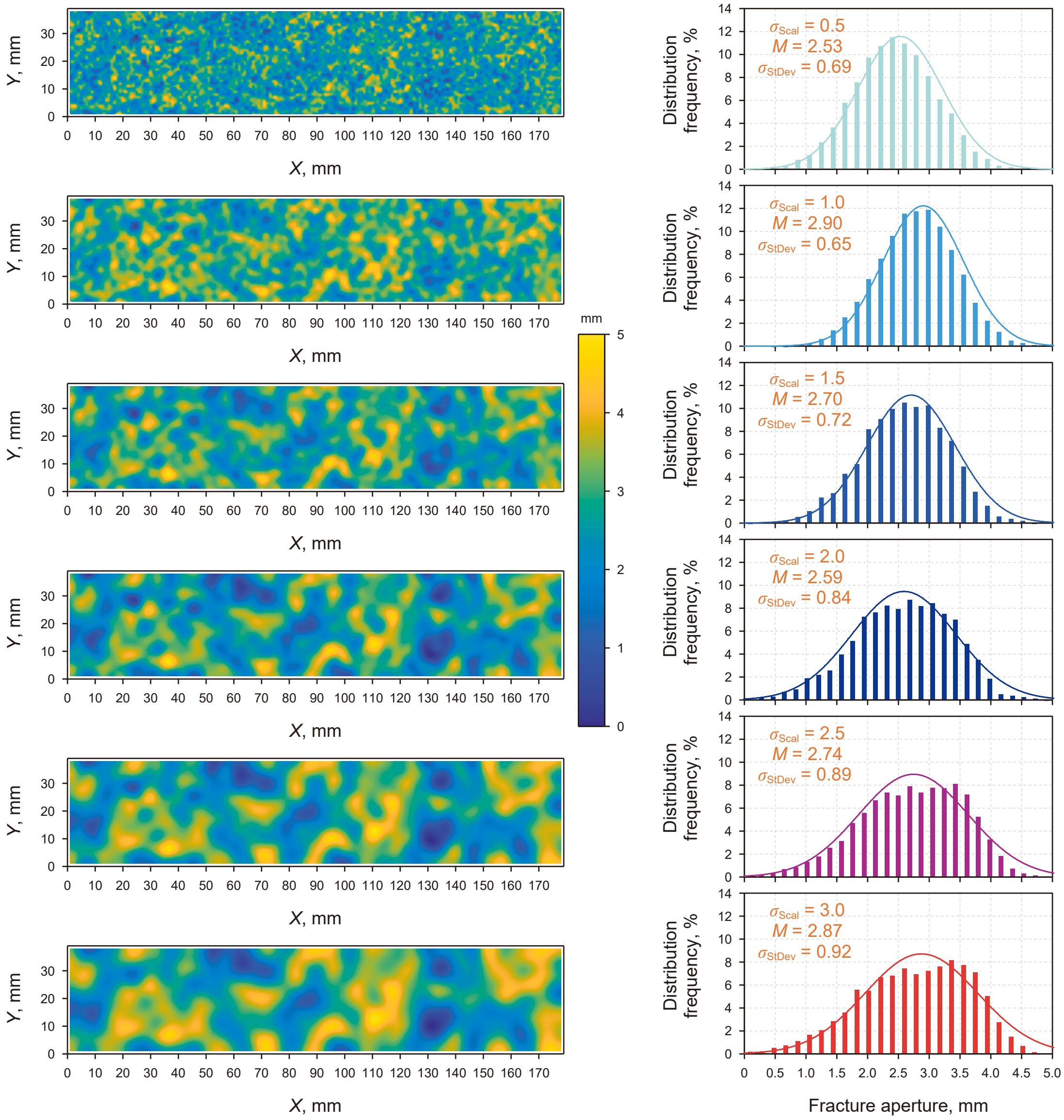

Fig. 15. Original fractures aperture and statistical characteristics with multi-scale rough structures.

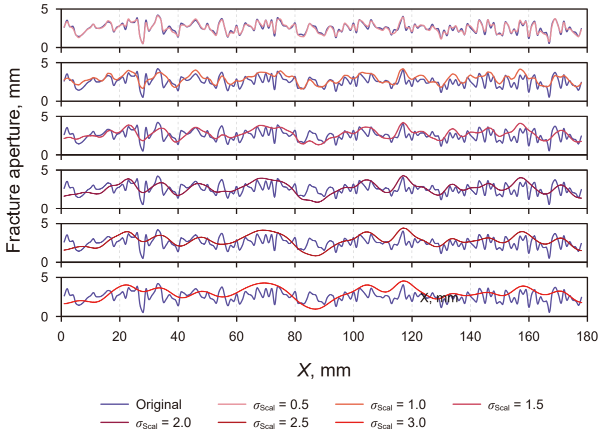

Fig. 16. The cross-sectional profile curves of fractures aperture with multi-scale rough structures.

configurations exhibit dual effects: they induce tortuous flow pathways, increasing the actual flow distance and flow accumulation, while simultaneously engendering specialized hydrodynamics phenomena such as “diffusion flow” and “reverse flow”. These phenomena increase fluid flow resistance and reduce fracture conductivity. This mechanistic analysis demonstrates that the conductivity of self-propping fractures under closure stress cannot be assessed solely based on fractures width as an independent criterion, comprehensive consideration of these complex structural characteristics is necessary.

4.4. Effect of multi-scale morphology on conductivity in rough-walled fractures

The morphological complexity of fractures is inherently characterized by multi-scale surface roughness. Through hierarchical decomposition and reconstruction of these multi-scale features, the systematic influence of morphological heterogeneity on rough

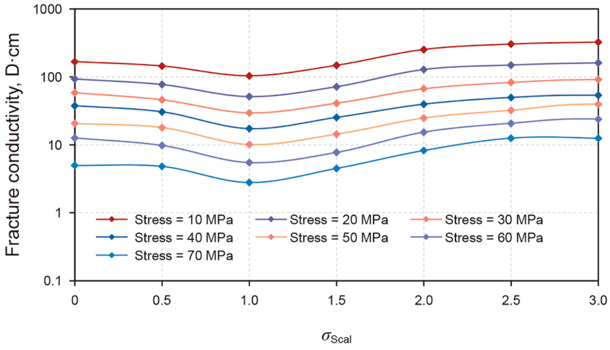

Fig. 17. Variation of fracture conductivity multi-scale rough structures.

fracture transmissibility can be quantitatively evaluated. In this investigation, Gaussian low-pass filtering was employed to deliberately segment and recombine fracture roughness. A two-dimensional Gaussian distribution function (Eq. (22)) was employed as the kernel function, whose scale parameter was deliberately modulated. Direct convolution was applied to the original aperture distribution field, generating restructured aperture fields incorporating roughness at multiple discrete scales:

$$\varphi(x,y)=\frac{1}{\sigma_{\mathrm{Scal}}\sqrt{2\pi}}\times\exp\left[\left(-\frac{x^2+y^2}{2\sigma_{\mathrm{Scal}}{}^2}\right)\right]. \tag{22}$$

where, (x, y) is the coordinates to the center of the Gaussian function; σ_{Scal} is the scale parameter governing the scale of roughness.

Based on the original fractures aperture distribution characterized by a fractal dimension of $F_{\mathrm{D}} = 2.7$ as the fundamental template, we systematically adjusted the scale parameters (σ_{Scal}) values of 0.5, 1.0, 1.5, 2.0, 2.5, and 3.0. This process yielded the reconstructed fractures aperture distributions presented in Fig. 15. Statistically, the aperture distributions incorporating multi-scale rough structures remain confined to the range of 0–5 mm. The

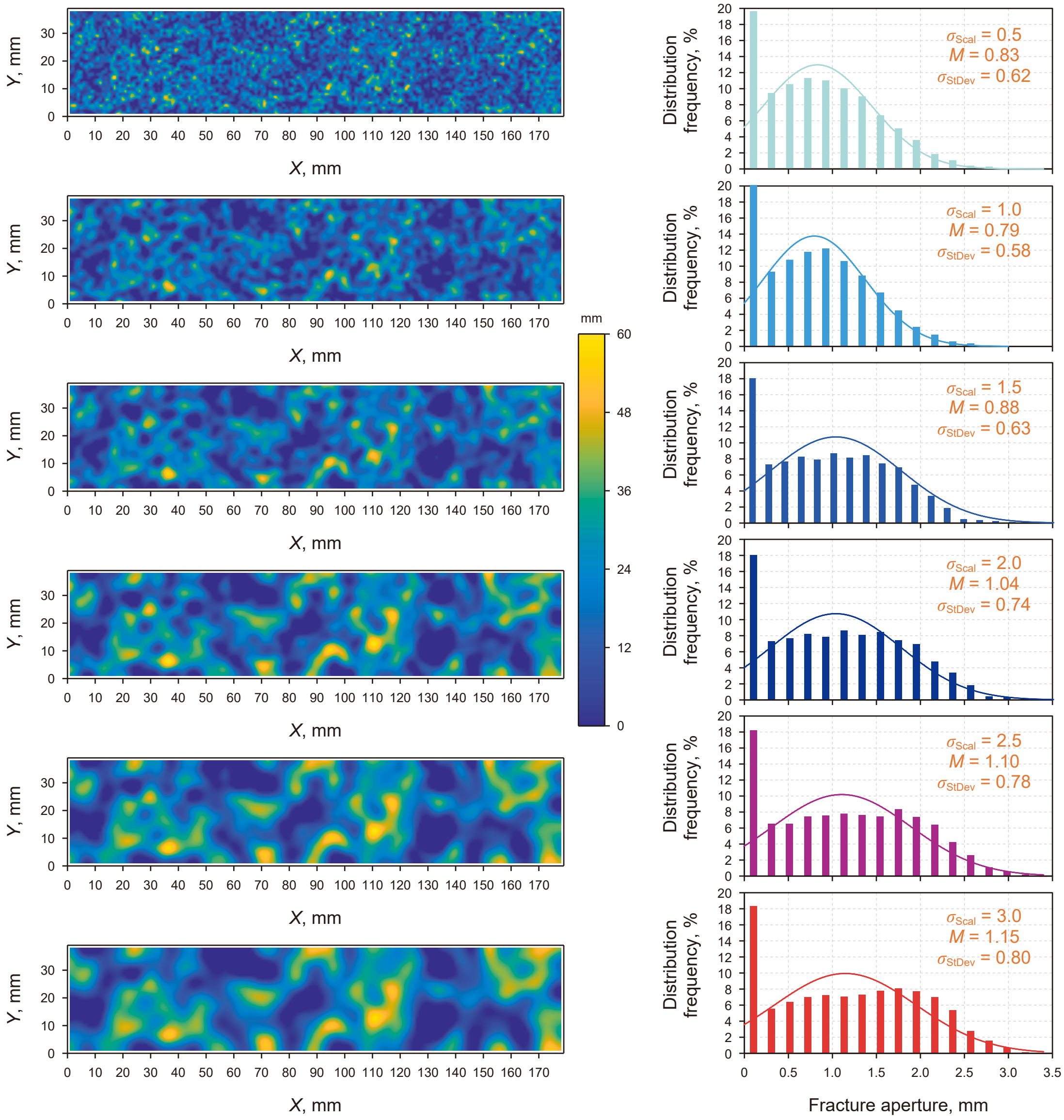

Fig. 18. Fractures aperture and statistical characteristics with multi-scale rough structures under closure stress of 40 MPa.

mean aperture value range from 2.53 to 2.90 mm, with standard deviations spanning 0.65 to 0.92. The decomposition and reconstruction of rough structures across different scales induce significant variations in mean aperture among the fracture sets. Concurrently, the aperture distributions progressively deviate from a normal distribution. Regarding distribution patterns, the reconstructed fracture spaces exhibit increasing smoothness with ascending scale parameters, where regions characterized by larger and smaller apertures also demonstrate progressive localization. Fracture aperture profile curves derived from sampling path data along the X-axis at $Y = 19$ mm are presented in Fig. 16. The scale parameter exhibits a positive correlation with the spatial fluctuation wavelength of these aperture profile curves. When the scale parameter assumes larger values, the aperture distribution within the reconstructed fracture medium is dominated by the preservation of coarser-scale rough features. Conversely, the assignment of smaller scale parameter values renders finer-scale textural features within the reconstructed fracture medium increasingly discernible, revealing enhanced resolution of microstructural heterogeneities.

Based on the reconstructed fractures aperture distribution, flow simulation under varying closure stresses were conducted, with the corresponding results presented in Fig. 17. The results demonstrate that under identical closure stress conditions, the conductivity of self-propping fractures exhibits a tri-phasic trend characterized by “an initial decline, followed by an increase, and subsequent decline” as the scale parameter varies. When scale parameters are $\sigma_{\mathrm{Scal}} = 0.5$ and $\sigma_{\mathrm{Scal}} = 1$, the decomposition and reconstruction of rough structures did not significantly alter the spatial fluctuation characteristics of the fracture aperture profiles (see Fig. 16). However, this process eliminated certain high-aperture “peaks” and low-aperture “valleys” at fluctuating positions, resulting in insufficient effective support under closure stress. This led to substantial increased fracture deformation and reduced fractures aperture (as shown in Fig. 18). Concurrently, non-contacting rough structures within fractures continued to exert notable influences on fluid flow, manifesting as highly heterogeneous velocity magnitudes and directions that consequently diminished conductivity of self-propping fractures. As the scale parameter increased, recombined larger-scale rough structures

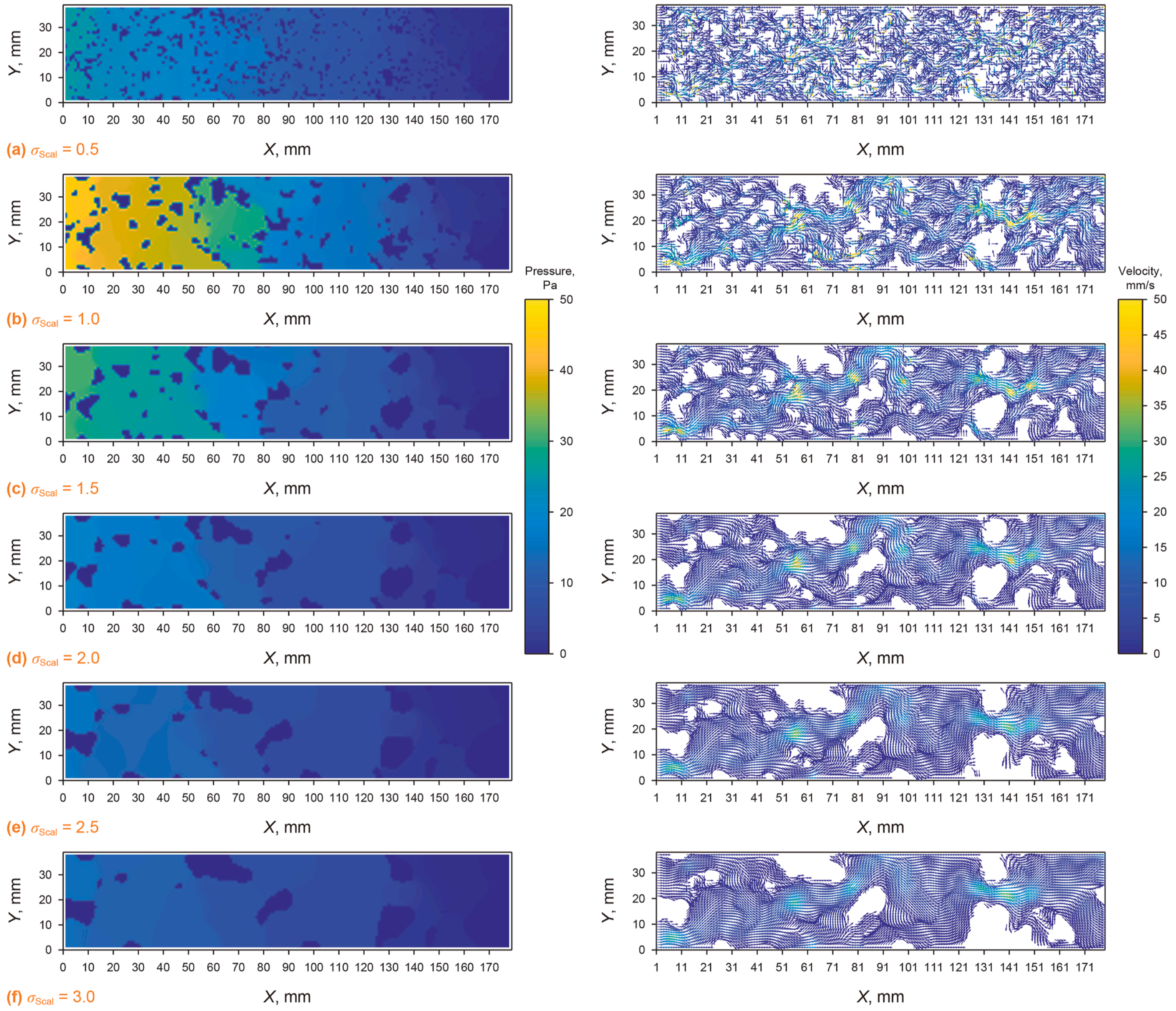

(a) $\sigma_{\mathrm{Scal}} = 0.5$

(b) $\sigma_{\mathrm{Scal}} = 1.0$

(c) $\sigma_{\mathrm{Scal}} = 1.5$

(d) $\sigma_{\mathrm{Scal}} = 2.0$

(e) $\sigma_{\mathrm{Scal}} = 2.5$

(f) $\sigma_{\mathrm{Scal}} = 3.0$

Fig. 19. The pressure fields and flow fields distribution characteristics in fractures with multi-scale rough structures under closure stress of 40 MPa.

exhibited progressively smoother fractures aperture profiles. The formation of "cluster-like" contacting micro-asperities significantly enhanced fracture deformation resistance. Simultaneously, smaller-scale roughness features diminished during scale parameter evolution, reducing surface roughness effects on fluid flow. Residual non-contacting micro-asperities exerted negligible impacts on intra-fracture flow, promoting the gradual recovery and enhancement of fracture conductivity. The conductivity reached its maximum value at a scaling parameter of $\sigma_{\text{Scal}} = 3$. With further increases in scale parameter, fracture surfaces retained only essential roughness elements, rendering fracture space increasingly smooth. Progressive surface smoothing facilitated the development of "throat-shaped" constriction geometries, particularly under elevated closure stress conditions. At a high closure stress of 70 MPa, these throat-dominated structures became predominant in governing fluid transport dynamics. This transition resulted in a paradoxical conductivity reduction at $\sigma_{\text{Scal}} = 3$ compared to $\sigma_{\text{Scal}} = 2.5$, despite the initial conductivity recovery trend. This phenomenon arises from the competitive interaction between the roughness-mediated flow resistance reduction and the throat constriction effects during mechanical compression.

Further analysis of fluid pressure and velocity field distributions within reconstructed fractures was performed, as illustrated in Fig. 19. As the scale parameter increases, the clustering characteristics of contact micro-asperities formed within fractures exhibit increasingly pronounced aggregation tendencies. These contact zones impose increasingly significant constriction on fracture flow channels through the accumulation of contact micro-asperities, generating substantial pressure drops between adjacent high-density "cluster-like" contact micro-asperities aggregates. This phenomenon constitutes the primary source of fluid flow resistance. From the flow field perspective, increasing the scale parameter causes high-density "cluster-like" contact micro-asperities to meander the fluid flow path and establish dominant primary flow channels. However, with diminishing retention of rough structural details within the fracture, the fluid flow within these primary channels becomes more uniform and consolidated. For fractures restructured with multiscale roughness, the spatial configuration of the primary flow pathways remains fundamentally consistent. This indicates that primary flow pathways in self-propping fractures are predominantly governed by large-scale foundational roughness structures. In contrast, smaller-scale roughness features merely enhance flow heterogeneity in velocity magnitude and direction through localized flow phenomena such as circumfluent flow, diffusion flow, and reverse flow. Critically, these secondary structures do not alter the spatial distribution pattern of the primary flow channels in self-propping fractures.

5. Conclusions

This study focuses on the regulatory effects and underlying mechanisms of rough fracture morphology on the stress-flow coupled evolution of self-propping fractures in shale. Particular attention is given to investigating how microscopic alterations in fracture morphology govern macroscale fracture flow capacity. The principal conclusions drawn from this research are as follows.

(1) Under closure stress, the deformation increment in self-propping fractures demonstrates a pronounced synchronous response with fracture conductivity degradation. Moreover, a distinct linear positive correlation exists between the extent of deformation and the magnitude of conductivity reduction as closure stress intensifies. The progressive narrowing of self-propping fractures aperture under increasing closure stress represents the primary mechanism driving persistent fracture conductivity deterioration.

(2) The fractal dimension demonstrates a linear positive correlation with fracture conductivity. Although increased fractal dimension creates more complex rough structural features capable of impeding flow, the application of closure stress induces significant reconfiguration of flow channels within the fractures space. Crucially, these morphological irregularities enhance the stress disturbance resistance of the fracture architecture. Compressive stress loading preserves primary conductive pathways through mechanical stabilization. This counterintuitive phenomenon fundamentally arises from the stress-driven geometric optimization mechanism. The synergistic interaction between fractal roughness and stress-mediated deformation promotes advantageous reconfiguration of flow conduits, rather than solely exerting obstructive effects.

(3) The conductivity of self-propping fractures under closure stress cannot be evaluated solely based on fractures width as an independent criterion. Both high-density "cluster-like" contact micro-asperities and "throat-shaped" constriction structures constitute critical factors requiring focused investigation. Specifically, regions formed by high-density "cluster-like" contact micro-asperities significantly constrict flow pathways within the fracture, inducing specialized flow phenomena such as "transverse flow" and "reverse flow". Concurrently, "throat-shaped" constriction structures generate substantial throttling effects, triggering abrupt pressure drops. These combined mechanisms demonstrably impair the conductivity of self-propping fractures under closure stress.

(4) Fractures exhibiting lower roughness tend to develop "throat-shaped" constriction structures under closure stress. Within these structures, the fracture conductivity is governed by the competing interplay between roughness-mediated reduction in flow resistance and the flow-constricting effect of throat narrowing during mechanical compression. The primary flow pathways in self-propping fractures are primarily determined by fundamental, large-scale rough structures. In contrast, the small-scale roughness features merely induce heterogeneity in the flow field's velocity magnitude and direction. Crucially, these secondary structures do not fundamentally alter the spatial distribution of primary flow channels in self-propping fractures.

CRediT authorship contribution statement

Ming-Yong Zeng: Writing – original draft, Methodology, Investigation, Conceptualization. **Hang-Yu Zhou:** Writing – review & editing, Methodology, Conceptualization.

Declaration of competing interest

The authors declare that they have no known competing financial interests or personal relationships that could have appeared to influence the work reported in this paper.

References

Aliu, A., Xie, L., He, S., 2022. A model to describe hydraulic fracture conductivity decline curve in 3-stages focus on Longmaxi Formation. J. Nat. Gas Sci. Eng. 100, 104458. https://doi.org/10.1016/j.jngse.2022.104458.

Britt, L.K., Smith, M.B., Haddad, Z., 2006. Water-fracs: We do need proppant after all. In: SPE Annual Technical Conference and Exhibition. https://doi.org/10.2118/102227-MS.

Baghbanan, A., Jing, L., 2008. Stress effects on permeability in a fractured rock mass with correlated fracture length and aperture. Int J Rock Mech Min 45 (8), 1320–1334. https://doi.org/10.1016/j.ijrmms.2008.01.015.

Blöcher, G., Kluge, C., Milsch, H., 2019. Permeability of matrix-fracture systems under mechanical loading–constraints from laboratory experiments and 3-D numerical modelling. Adv. Geosci. 49, 95–104. https://doi.org/10.5194/adgeo-49-95-2019.

Chen, C., 2022. Numerical Calculation Studies of Shale self-propped Fracture Conductivity. Master Thesis. China University of Petroleum (Beijing) (in Chinese).

Chen, C., Wang, S., Lu, C., 2021. An experimental investigation of hydraulic fracture conductivities in shales. In: 55th U.S. Rock Mechanics/Geomechanics Symposium. ARMA 21-1323.

Chen, T., Feng, X.T., Cui, G., 2019. Experimental study of permeability change of organic-rich gas shales under high effective stress. J. Nat. Gas Sci. Eng. 64, 1–14. https://doi.org/10.1016/j.jngse.2019.01.014.

Cheng, L., Rong, G., Yang, J., 2017. Fluid flow through single fractures with directional shear dislocations. Transport Porous Media 118 (2), 1–26. https://doi.org/10.1007/s11242-017-0861-9.

Cheng, Z., Liu, S., Shi, A., 2024. Effect of fractal surface roughness and pressure gradient on the hydraulic behavior of fluid flow through a 3D single rough fracture. Eur J of Environ Civ En 28 (5), 1104–1117. https://doi.org/10.1080/19648189.2023.2243502.

Cipolla, C.L., Lolon, E.P., Mayerhofer, M.J., 2009. The effect of proppant distribution and un-propped fracture conductivity on well performance in unconventional gas reservoirs. In: SPE Hydraulic Fracturing Technology Conference. https://doi.org/10.2118/119368-MS.

Cunningham, D., Auradou, H., Shojaei-Zadeh, S., 2020. The effect of fracture roughness on the onset of non-linear flow. Water Resour. Res. 56, e2020WR028049. https://doi.org/10.1029/2020WR028049.

Deng, Q., Blcher, G., Cacace, M., 2021. Hydraulic diffusivity of a partially open rough fracture. Rock Mech. Rock Eng. 54 (10), 1–23. https://doi.org/10.1007/s00603-021-02629-2.

Dapp, W.B., Andreas, L., Persson, B., 2012. Self-affine elastic contacts: Percolation and leakage. Phys. Rev. Lett. 108 (24), 244301. https://doi.org/10.1103/PhysRevLett.108.244301.

Deng, Q., Jean, S., Mauro, C., 2024. Mechanical stiffness and permeability of a reservoir-scale rough fracture during closure. J. Geophys. Res. Solid Earth 129 (9), 2024JB029001. https://doi.org/10.1029/2024JB029001.

Finenko, M., Konietzky, H., 2024. Numerical simulation of turbulent fluid flow in rough rock fracture: 2D case. Rock Mech. Rock Eng. 57 (1), 451–479. https://doi.org/10.1007/s00603-023-03634-3.

Gou, X., 2017. Research on Numerical Method for Unpropped Fracture Conductivity of Shale. PhD Thesis. Southwest Petroleum University (in Chinese).

Guan, R., Huang, K., Zhou, C., 2012. A new constitutive law for the nonlinear normal deformation of rock joints under normal load. Sci. China Technol. Sci. 55 (2), 13. https://doi.org/10.1007/s11431-011-4654-z.

Guo, P., Wang, M., He, M., 2020. Experimental investigation on macroscopic behavior and microfluidic field of nonlinear flow in rough-walled artificial fracture models. Adv. Water Resour. 142, 103637. https://doi.org/10.1016/j.advwatres.2020.103637.

Guo, X., Wang, R., Shen, B., 2025. Geological characteristics, resource potential, and development direction of shale gas in China. Petrol. Explor. Dev. 52 (1), 15–28. https://doi.org/10.1016/S1876-3804(25)60002-4.

Hopkins, D.L., 2000. The implications of joint deformation in analyzing the properties and behavior of fractured rock masses, underground excavations, and faults. Int J Rock Mech Min 37 (1), 175–202. https://doi.org/10.1016/S1365-1609(99)00100-8.

Hu, X., Dong, E., Zhou, F., 2024. A new numerical model for simulation of flow on rough fracture. Geo En 234, 212540. https://doi.org/10.1016/j.geoen.2023.212540.

Huang, T., Zhai, C., Liu, T., 2025. Microstructural evolution and hydraulic response of shale self-propped fracture using X-ray computed tomography and digital volume correlation. Int. J. Min. Sci. Technol. 35, 345–362. https://doi.org/10.1016/j.ijmst.2025.02.005.

Huang, Y., Zhang, Y., Gao, X., 2021. Experimental and numerical investigation of seepage and heat transfer in rough single fracture for thermal reservoir. Geothermics 95, 102163. https://doi.org/10.1016/j.geothermics.2021.102163.

Jansen, T., Zhu, D., Hill, A.D., 2015. The effect of rock mechanical properties on fracture conductivity for shale formations. In: SPE Hydraulic Fracturing Technology Conference. https://doi.org/10.2118/SPE-173347-MS.

Jiang, B., Lu, C., Huang, C., 2020. A study on deformation characteristics of shale self-propped fracture under normal stress. In: 54th U.S. Rock Mechanics/Geomechanics Symposium. ARMA-2020-1744.

Julia, F., Gale, W., Stephen, E., 2014. Natural fractures in shale: A review and new observations. AAPG Bull. 98 (11), 2165–2216. https://doi.org/10.1306/08121413151.

Klimczak, C., Schultz, R.A., Parashar, R., 2010. Cubic law with aperture-length correlation: implications for network scale fluid flow. Hydrogeol. J. 18 (4), 851–862. https://doi.org/10.1007/s10040-009-0572-6.

Kong, B., Chen, S., 2018. Numerical simulation of fluid flow and sensitivity analysis in rough-wall fractures. J. Petrol. Sci. Eng. 168, 546–561. https://doi.org/10.1016/j.petrol.2018.04.070.

Koyama, T., Neretnieks, I., Jing, L., 2008. A numerical study on differences in using Navier-Stokes and Reynolds equations for modeling the fluid flow and particle transport in single rock fractures with shear. Int J Rock Mech Min 45 (7), 1082–1101. https://doi.org/10.1016/j.ijrmms.2007.11.006.

Kulatilake, P., Park, J., Su, X., 2020. Fluid flow through natural single-rock fractures: experimental and numerical investigations. Int. J. GeoMech. 20, 04020168. https://doi.org/10.1061/(ASCE)GM.1943-5622.0001790.

Lai, J., Guo, J., Wu, K., 2019. The effects of roughness and mechanical property of rough fracture surface on hydraulic fracture conductivity. In: 53rd U.S. Rock Mechanics/Geomechanics Symposium. ARMA-2019-2125.

Lee, S.H., Lee, K.K., Yeo, I.W., 2014. Assessment of the validity of Stokes and reynolds equations for fluid flow through a rough-walled fracture with flow imaging. Geophys. Res. Lett. 41 (13), 4578–4585. https://doi.org/10.1002/2014GL060481.

Li, B., Liu, R., Jiang, Y., 2019. An experimental method to visualize shear-induced channelization of fluid flow in a rough-walled fracture. Hydrogeol. J. 27 (8), 3097–3106. https://doi.org/10.1007/s10040-019-02048-2.

Li, M., Liu, X., Li, Y., 2022. Effect of contact areas on seepage behavior in rough fractures under normal stress. Int. J. GeoMech. 22 (4), 04022019. https://doi.org/10.1061/(asce)gm.1943-5622.0002330.

Li, W., Frash, L.P., Welch, N.J., 2021. Stress-dependent fracture permeability measurements and implications for shale gas production. Fuel 290 (9), 119984. https://doi.org/10.1016/j.fuel.2020.119984.

Li, Z., Mao, K., Liu, J., 2024. Analysis of fracture surface morphology and study of seepage diffusion characteristics. KSCE J. Civ. Eng. 28 (1), 428–443. https://doi.org/10.1007/s12205-023-0263-1.

Lu, C., Huang, C., Chen, C., 2019. Study on the flow mechanism simulation of deep shale propped fractures in Sichuan basin. In: 53rd U.S. Rock Mechanics/Geomechanics Symposium. ARMA-2019-0266.

Lu, C., Lu, Y., Gou, X., 2020. Influence factors of unpropped fracture conductivity of shale. Energy Sci. Eng. 8 (6), 2024–2043. https://doi.org/10.1002/ese3.645.

Lu, C., Luo, Y., Guo, J., 2021. Numerical investigation of unpropped fracture closure process in shale based on 3D simulation of fracture surface. J. Petrol. Sci. Eng. 208 (1), 109299. https://doi.org/10.1016/j.petrol.2021.109299.

Mandelbrot, B., Van, Ness J., 1968. Fractional Brownian motions, fractional noises and applications. SIAM Rev. 10, 422–437. https://doi.org/10.1137/1010093.

Medici, G., West, L.J., Banwart, S.A., 2019. Groundwater flow velocities in a fractured carbonate aquifer-type: Implications for contaminant transport. J. Contam. Hydrol. 222, 1–16. https://doi.org/10.1016/j.jconhyd.2019.02.001.

Nasvi, M., Ranjith, P., Sanjayan, J., 2013. Sub and super critical carbon dioxide permeability of wellbore materials under geological sequestration conditions: an experimental study. Energy 54 (2), 231–239. https://doi.org/10.1016/j.energy.2013.01.049.

Pentland, A.P., 2009. Fractal-based description of natural scenes. IEEE T Pattern Anal (6), 661–674. https://doi.org/10.1109/TPAMI.1984.4767591. PAMI-6.

Petrovitch, C.L., Pyrak-Nolte, L.J., Nolte, D.D., 2014. Combined scaling of fluid flow and seismic stiffness in single fractures. Rock Mech. Rock Eng. 47 (5), 1613–1623. https://doi.org/10.1007/s00603-014-0591-z.

Pyrak-Nolte, L., Morris, J., 2000. Single fractures under normal stress: The relation between fracture specific stiffness and fluid flow. Int J Rock Mech Min 37, 245–262. https://doi.org/10.1016/S1365-1609(99)00104-5.

Rodríguez, X., Barbosa, Cardona, A., 2024. Impact of carbonate content, rock texture, and roughness on fracture transmissivity and acid-etching patterns in carbonate rocks. Rock Mech. Rock Eng. 57 (9), 6683–6699. https://doi.org/10.1007/s00603-024-03901-x.

Rong, G., Tan, J., Zhan, H., 2020. Quantitative evaluation of fracture geometry influence on nonlinear flow in a single rock fracture. J. Hydrol. 589 (1−2), 125162. https://doi.org/10.1016/j.jhydrol.2020.125162.

Sharma, M.M., Manchanda, R., 2015. The role of induced un-propped (IU) fractures in unconventional oil and gas wells. In: SPE Annual Technical Conference and Exhibition. https://doi.org/10.2118/174946-MS.

Su, X., Zhang, T., Zhou, L., 2024. Experimental study on nonlinear flow behavior in smooth and rough sandstone fractures subjected to various injection pressure and normal compressive stress. Environ. Earth Sci. 83 (6), 171. https://doi.org/10.1007/s12665-023-11415-y.

Sun, H., Cai, X., Hu, D., 2023. Theory, technology and practice of shale gas three-dimensional development: A case study of Fuling shale gas field in Sichuan basin, SW China. Petrol. Explor. Dev. 50 (3), 573–584. https://doi.org/10.11698/PED.20220847.

Tzelepis, V., Moutsopoulos, K.N., Papaspyros, J.N.E., 2015. Experimental investigation of flow behavior in smooth and rough artificial fractures. J. Hydrol. 521 (2), 108–118. https://doi.org/10.1016/j.jhydrol.2014.11.054.

Wang, H., Ji, G., Chen, Y., 2024. A novel equivalent model of radionuclide migration in three-dimensional rough shear fractures. Int. J. Heat Mass Tran. 228 (8), 125646. https://doi.org/10.1016/j.ijheatmasstransfer.2024.125646.

Wei, S., Jin, Y., Wang, S., 2022. A framework to obtain the formulas of the conductivity and aperture of rough fractures under thermo-hydro-mechanical conditions. J. Petrol. Sci. Eng. 208, 109354. https://doi.org/10.1016/j.petrol.2021.109354.

Wu, K., 2019. Study on Artificial Fracture Conductivity of Shale Reservoir Based on Fracture Surface Reconstruction. Master Thesis. Southwest Petroleum University (in Chinese).

Wu, M., Jiang, C., Deng, B., 2024. Characterization and reconstruction of rough fractures based on vector statistics. Geo En 234, 212664. https://doi.org/10.1016/j.geoen.2024.212664.

Wu, W., Zhou, J., Kakkar, Pratik, 2019. An experimental study on conductivity of unpropped fractures in preserved shales. SPE Prod. Oper. 34, 280–296. https://doi.org/10.2118/184858-PA.

Xia, B., Huang, J., Peng, J., 2024. The evolution of geometry and flow characteristics of fracture inside tight sandstone under stress. Arch. Appl. Mech. 94 (4), 903–919. https://doi.org/10.1007/s00419-024-02555-z.

Xiao, F., Zhao, Z., 2019. Evaluation of equivalent hydraulic aperture (EHA) for rough rock fractures. Can. Geotech. J. 56 (10), 1486–1501. https://doi.org/10.1139/cgj-2018-0274.

Xie, J., Gao, M., Zhang, R., 2020. Experimental investigation on the anisotropic fractal characteristics of the rock fracture surface and its application on the fluid flow fescription. J. Petrol. Sci. Eng. 191 (3–4), 107190. https://doi.org/10.1016/j.petrol.2020.107190.

Xiong, F., Jiang, Q., Ye, Z., 2018. Nonlinear flow behavior through rough-walled rock fractures: The effect of contact area. Comput. Geotech. 102, 179–195. https://doi.org/10.1016/j.compgeo.2018.06.006.

Xu, C., Lin, C., Kang, Y., 2018. An experimental study on porosity and permeability stress-sensitive behavior of sandstone under hydrostatic compression: Characteristics, mechanisms and controlling factors. Rock Mech. Rock Eng. 51 (B04203), 2321–2338. https://doi.org/10.1007/s00603-018-1481-6.

Xu, W., Chen, R., Zhuang, L., 2024. Effects of roughness on density-driven convection of dissolved CO_2 in discrete fracture-matrix system. Comput. Geotech. 166 (2), 105996. https://doi.org/10.1016/j.compgeo.2023.105996.

Yang, B., Ma, W., Pan, G., 2024. Three-dimensional fracture space characterization and conductivity evolution analysis of induced un-propped fractures in shale gas reservoirs. Pet. Sci. 21 (6), 4248–4261. https://doi.org/10.1016/j.petsci.2024.07.022.

Yang, J., Wang, Z., Liu, L., 2023. Effects of roughness and aperture on mesoscopic and macroscopic flow characteristics in rock fractures. Environ. Earth Sci. 82 (24), 594. https://doi.org/10.1007/s12665-023-11290-7.

Zeng, M., Zhou, H., 2025. Investigation of acid-etching evolution in natural fractures of carbonate reservoirs under high closure stress. SPE J. 30 (1), 98–110. https://doi.org/10.2118/223952-PA. SPE-223952-PA.

Zhan, L., Hu, Y., Zou, L., 2022. Effects of multiscale heterogeneity on transport in three-dimensional fractured porous rock with a rough-walled fracture network. Comput. Geotech. 148, 104836. https://doi.org/10.1016/j.compgeo.2022.104836.

Zhang, X., Sanderson, D.J., 1996. Effects of stress on the two-dimensional permeability tensor of natural fracture networks. Geophys. J. Int. 125 (3), 912–924. https://doi.org/10.1111/j.1365-246X.1996.tb06034.x.

Zhao, Y., Wang, C., Bi, J., 2020. Analysis of fractured rock permeability evolution under unloading conditions by the model of elastoplastic contact between rough surfaces. Rock Mech. Rock Eng. 53 (12), 5795–5808. https://doi.org/10.1007/s00603-020-02224-x.

Zhong, Z., Wang, L., Song, L., 2021. Size effect on the hydraulic behavior of fluid flow through a single rough-walled fracture. Soil Dynam. Earthq. Eng. 143 (11), 106615. https://doi.org/10.1016/j.soildyn.2021.106615.

Zhou, J., Zhang, L., Li, X., 2019. Experimental and modeling study of the stress-dependent permeability of a single fracture in shale under high effective stress. Fuel 257, 116078. https://doi.org/10.1016/j.fuel.2019.116078.

Zhou, Z., Zhang, J., Cai, X., 2020. Permeability evolution of fractured rock subjected to cyclic axial load conditions. Geofluids 1–12. https://doi.org/10.1155/2020/4342514.

Zhu, W., Lei, G., He, X., 2022. Can we infer the percolation status of 3D fractured media from 2D outcrops? Eng. Geol. 302, 106648. https://doi.org/10.1016/j.enggeo.2022.106648.

Zou, L., Jing, L., Cvetkovic, V., 2017. Shear-enhanced nonlinear flow in rough-walled rock fractures. Int J Rock Mech Min 97, 33–45. https://doi.org/10.1016/j.ijrmms.2017.06.001.